PeerJ Materials Science

Microwave assisted synthesis of bismuth titanate nanosheets and its photocatalytic effects

Adrine Antony Correya, V. P. N. Nampoori and A. Mujeeb

International School of Photonics, Cochin University of Science and Technology, Kochi, Kerala, India

ABSTRACT

Bismuth titanate syntheses using wet chemical methods are comparatively time-consuming and require long durations for completion using the well-studied sol-gel method. In this work, we use microwave initiated combustion method to produce ultra-thin bismuth titanate nanosheets. This method reduces the time required for the synthesis down to minutes, when compared to hours or days in most other methods. The thickness of the synthesized sheets were tuned by adding polyethylene glycol as a capping agent, which in turn affects the band gap and subsequently, their photocatalytic properties. The samples were characterized using x-ray diffraction, transmission electron microscopy and absorption spectrophotometry. Photocatalytic effect of the synthesized bismuth titanate nanosheets on methylene blue dye also studied and variation of band gap depending on thickness of the nanosheets were observed.

Subjects Electronic, Optical and Magnetic, Nano and Microstructured Materials
Keywords Microwave synthesis, Bismuth titanate, Photocatalysis, Band gap

INTRODUCTION

Bismuth titanates are a large class of compounds of metal oxides of bismuth and titanium. Most of these materials characterize a perovskite-like crystal structure with alternating layers of $Bi_2O_2^+$ and $M_{n-1}Ti_nO_{3n+1}^{m+}$ where M is a metal atom (*Newnham, Wolfe & Dorrian, 1971*). These materials display a wide variety of physical properties, both in bulk as well as in the nano regime, depending on the metal M (*Chiang, Farrey & Soukhojak, 1998*; *Koroleva et al., 2013*; *Ramana et al., 2017*). Bismuth titanate in the simplest form has Ti replacing M, resulting in $Bi_4Ti_3O_{12}$ which characterize a perovskite structure which was first reported in 1949 by *Aurivillius (1949)*. Other two phases of this compound are pyrochlore ($Y_{x-1}Bi_xTi_2O_7$, Y = Ti) and sillenite ($Bi_{12}TiO_{24}$) (*Skorikov et al., 2005*; *Noureldine et al., 2015*; *Lanfredi & Nobre, 2005*). These are well known for characteristics like ferro, piezo and pyroelectric effects used in various applications including photovoltaics and photocatalysis (*Lazarević, Stojanović & Varela, 2005*).

Photocatalysis is a well-studied method to break down long-chain effluents, pollutants and even microbes in wastewater (*Sunada et al., 1998*). Photocatalysis infrastructure plays a major role in treating and recycling wastewater from various chemical and bio-hazard facilities utilizing abundantly available solar energy. Seminal studies and implementation

Submitted 25 October 2021
Accepted 30 December 2022
Published 7 March 2023

Corresponding author
Adrine Antony Correya,
acorreya@cusat.ac.in

Academic editor
Junkuo Gao

Additional Information and Declarations can be found on page 9

DOI **10.7717/peerj-matsci.26**

of photocatalysis pertaining to the Honda-Fujishima effect were reported using titanium dioxide owing to its high photocatalytic activity under the ultraviolet spectrum of solar irradiation (*Hashimoto, Irie & Fujishima, 2005*). Various other semiconductor nanocomposites have been since proposed to make better use of the solar spectra which mostly include ceramic oxides of metals like zinc, tungsten, *etc.* (*Khan, Adil & Al-Mayouf, 2015*; *Maji et al., 2012*; *Park, Park & Kim, 2006*; *Zhao & Miyauchi, 2008*).

Study of photocatalysis using bismuth titanate composites gained traction with research since the early 2000s owing to its capability of degrading dyes and eliminating microbes under visible light irradiation. This material is one of the major contributors towards bringing down the spectral sensitivity of photocatalysts below the ultraviolet region of the solar spectrum, making better use of the visible spectrum (*Yao et al., 2003*; *Natarajan et al., 2013*; *Wei, Dai & Huang, 2009*; *Zambrano et al., 2017*). Various bismuth titanate composites were also band engineered by tuning its crystalline phases, particle size and morphologies as well as by doping various elements to achieve precise characteristics appropriate for applications like photocatalysis, ferroelectrics and photovoltaics (*Chen et al., 2016*; *Murugesan et al., 2010*; *Kong et al., 2008*; *Zhou et al., 2007*).

The most studied synthesis methods reported for bismuth titanate with engineered band gap include solvothermal, sol-gel and solid-state routes. It has also been reported that bismuth titanate in the perovskite phase shows improved photocatalytic effects when they are textured along the (001) plane (*Zhao et al., 2013*; *Dawley et al., 2001*). This texture reveals as a sheet-like formation due to the perovskite crystalline nature of the Aurivillius bismuth titanate phase (*Sardar & Walton, 2012*; *Chen, Li & Zhang, 2011*). This work discusses the use of a quick microwave-initiated combustion synthesis of perovskite $Bi_4Ti_3O_{12}$ nanosheets textured along the (001) plane and its photocatalytic efficiency in degrading methylene blue dye.

MATERIALS AND METHODS

The bismuth titanate (BTO) nanosheets were synthesized by reacting stoichiometric amounts of bismuth and titanium precursors by microwave irradiation (*Pirgholi-Givi, Farjami-Shayesteh & Azizian-Kalandaragh, 2019*; *Yang et al., 2013*). The following reagents were used for the precursors as procured Bismuth nitrate pentahydrate ($(Bi(NO_3)_3)5H_2O$, 99%; MERC, Mumbai, Maharashtra), glacial acetic acid (CH_3COOH, 99%; Spectrachem, Lodi, NJ, USA), titanium tetraisopropoxide ($(Ti\{OCH(CH_3)_2)\}_4$, 98%; Acros Organics, Geel, Belgium), acetylacetone ($C_5H_8O_2$, 99%; Loba Chemie, Mumbai, Maharashtra) and polyethylene glycol (PEG-6000, 99%; Thermo Fischer Scientific, Waltham, MA, USA) were used in the synthesis.

The bismuth and titanium precursors used to synthesize bismuth titanate were prepared as follows. 5 g bismuth salt was dissolved in 4 mL glacial acetic acid and 1 mL pure water in room temperature under constant stirring. 0.79 mL titanium isopropoxide was dissolved dropwise in 0.55 mL acetylacetone under constant stirring in a cold bath to keep check of precipitation during the exothermic dissolution process. An extra 10% weight of Bi salt is added to the solution to compensate evaporation of bismuth during the synthesis (*Thiruramanathan et al., 2016*). The solutions were mixed in the appropriate volume ratios

to create three sets of samples, to which 0.02, 0.04 and 0.06 g of polyethylene glycol were added.

These samples were then irradiated in an 800 W commercial microwave for 30 s in open glass beakers. The irradiation caused the precursor fluid to expand and then dry up, resulting in light yellow foams during the first 10 s of microwave irradiation. The reaction then proceeded to a combustion stage where the foams scintillate quickly over the whole volume producing brown nitrate fumes. The reaction ended completely after 30 s of irradiation resulting in soft, flaky, pale yellow nanocomposite ash. The samples were thoroughly washed multiple times in water, ethanol and acetone to remove residual material. These were then heated to 500 °C for 30 min to remove any organic residues and to obtain a stable crystalline structure (*Du et al., 2008*; *Pirgholi-Givi, Farjami-Shayesteh & Azizian-Kalandaragh, 2019*). The samples were then ground to fine powder using a pestle and mortar and stored.

The prepared samples were marked as A, B and C depending on the amount of PEG added to the precursor before the synthesis, 0.02, 0.04 and 0.06 g respectively. These samples were characterized for crystalline phases using X-ray diffraction (XRD) with the Bruker AXS D8 Advance over the range 10° to 80° with a 2θ resolution of 0.08°. The TEM images of the samples were captured using a Jeol JEM 2100 to a scale of 5 nm. The UV-Vis absorption spectra of the samples were recorded using a Jasco 570 spectrophotometer within the wavelength range of 850 to 190 nm. CHNS analysis to determine the amount of residual carbon and other residual elements using the Elementar Vario EL III. The data from experiments were analyzed using the IPython and NumPy packages (*Hunter, 2007*; *Perez & Granger, 2007*) and plots were generated using the Matplotlib package (*Harris et al., 2020*).

A control sample of bismuth titanate was synthesized by the sol-gel method for comparison of photocatalysis and is labelled as K (*Yao et al., 2003*). Known amounts of these dispersions were mixed with measured quantities of methylene blue (MB) dye solution and irradiated with a 1,000 W Xenon lamp for measuring the photodegradation effects.

RESULTS

The fine powdered samples were characterized for crystalline nature using XRD and the patterns were search-matched using the Full Profile Search Match (FPSM) tool (*Lutterotti et al., 2019*; *Lutterotti, 2012*). Refining was done using the Maud package (*Lutterotti et al., 2007*). The XRD pattern of the samples A, B and C are depicted in Fig. 1. Search-match on the recorded patterns confirm the presence of bismuth titanate in perovskite phase having strongest lines of JCPDS 35-0795 seen in various reports including the seminal report (*Pirgholi-Givi, Farjami-Shayesteh & Azizian-Kalandaragh, 2019*; *Nogueira et al., 2014*; *Chen, Li & Zhang, 2011*; *Yi et al., 2009*). Traces of bismuth oxides (JCPDS 77-0374) were also detected and estimated to be less than 7%. This can be attributed to the extra bismuth precursor added for compensating evaporation losses (*Zarycka et al., 2005*).

The estimated crystallite sizes for the particles using the Debye-Scherrer equation $d = k\lambda/\beta\cos\theta$ on the most prominent peak (117) are 18, 41 and 51 nm for samples A, B

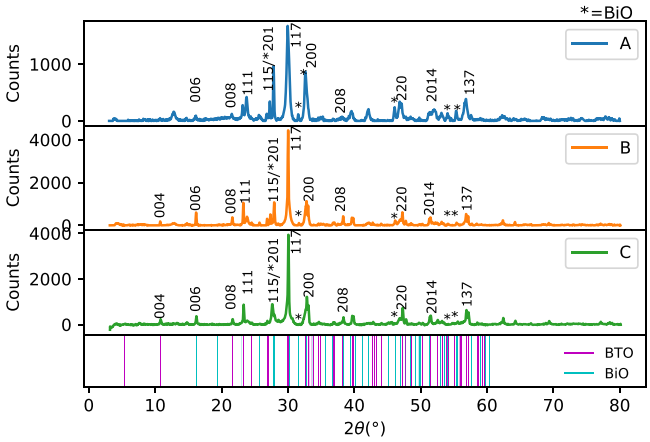

Figure 1 X-ray diffraction pattern of BTO samples (A), (B) and (C) prepared by varying PEG-6000 added during synthesis with matching lines for $Bi_4Ti_3O_{12}$ JCPDS 35-0795 and minute traces of Bi_2O_3 JCPDS 77-0374. The bottom subplots show the prominent peaks of JCPDS files 35-0795 (BTO) and 77-0374 (BiO), where the thickness of the line corresponds to the prominence of the peak. The Bi_2O_3 peaks are marked with an asterisk (*) instead of indices.

Full-size DOI: 10.7717/peerj-matsci.26/fig-1

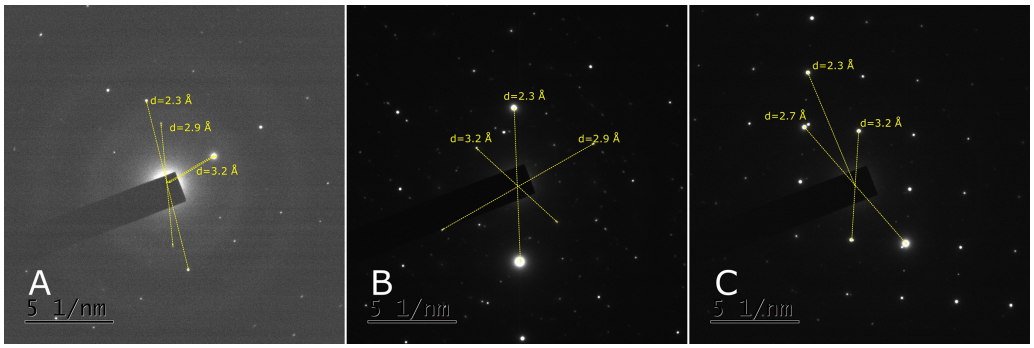

Figure 2 SAED pattern of BTO samples (A), (B) and (C) show the variation in crystallinity increasing with the addition of PEG-6000 during the synthesis. 2C shows the <117> plane of 2.7 Å spacing gaining prominenece with single crystallite-like features. The crystal planes measured on the SAED planes match those of bismuth titanate; a = 2.3 Å, b = 2.9 Å and c = 3.2 Å.

Full-size DOI: 10.7717/peerj-matsci.26/fig-2

and C respectively (*Cullity & Stock, 2014*; *Langford & Wilson, 1978*). This plane corresponds to the lateral dimension of the sheets and the crystallite sizes correlate roughly to the dimensions along the a-b axes.

The SAED patterns of the samples depicted in Fig. 2 confirms in conjunction with the XRD patterns, that the variation in crystallinity between the samples as well as the d-spacing corresponding to the prominent 2θ peaks in the XRD pattern. It can also be noted that the crystalline nature of the individual sheets tends to form single crystallites for samples B and C, with little broadening of diffracted X-rays. It can be noted that Fig. 2C shows the presence of 2.7 Å planes together with the 2.9 Å showing that the (00L) plane gaining prominence with the strongest (117) peak. The prominent diffraction spots match

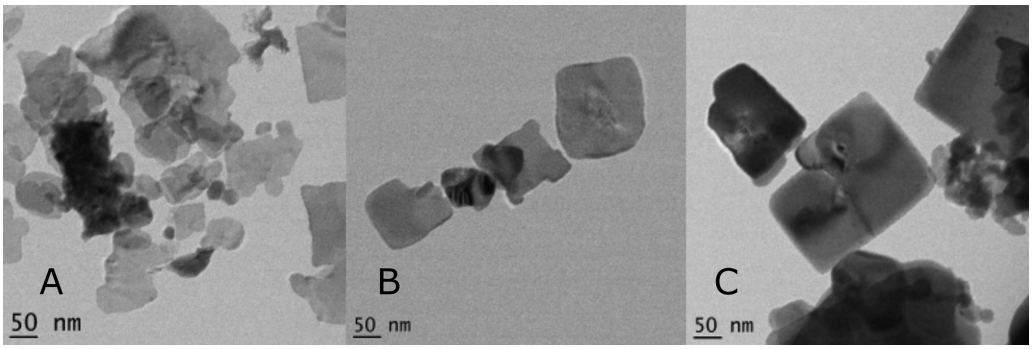

Figure 3 TEM recordings of BTO samples (A), (B) and (C) shows their sheet-like morphology. The thickness of the sheet increases depending on the PEG-6000 added before synthesis (A) having 0.02 g, (B) having 0.04 g and (C) having 0.06 g of PEG-6000 respectively. Sample A shows a mixture of sheets and agglomerated spheroids. The thickness of the sheets increase with the amount of PEG, showing the effect of the surfactant on the synthesis. Full-size DOI: 10.7717/peerj-matsci.26/fig-3

with the prominent peaks in XRD. Samples tend to show single crystallite like features with the increase in amount of PEG.

The TEM images depicted in Fig. 3 reveal the rectangular sheet morphology of the bismuth titanate nanostructures with nanometer thickness. The lateral dimensions are found to be up to around 100 to 200 nm while the thickness of the sample increases with the increase in the amount of PEG-6000 added to the precursor before synthesis, matching the XRD patterns recorded. This corresponding increase can be attributed to the effects of the capping agent controlling the lateral growth over the (001) axis of the bismuth titanate crystallite (*Bakshi, 2015*; *Kubiak et al., 2020*). The thickness of the nanosheets could not be determined using TEM due to practical limitations.

CHNS analysis of the samples show the presence of at most 0.84% C, 0.08% N and 0.02% H. This confirms that the capping agent was virtually absent in the sample and was completely incinerated and washed away. It can thus be stated that the PEG acts as a template agent providing nucleation and capping assisting the growth of the BTO nanosheets. All other residual material including nitrates and organic compounds can be considered absent.

The UV-visible absorbance spectra of A, B and C are depicted in Fig. 4. All samples have a familiar wide absorbance over the visible region as well as a peak at around 260 and 220 nm, which are well-known characteristics of bismuth titanate. The gradual rise of the absorbance curve denotes that the samples have a direct band gap. This has been identified and estimated by plotting hν against $(\alpha h\nu)^2$ where the values fit linearly to the equation $(\alpha h\nu)^2 = A(h\nu - E_g)$ showing allowed direct band gap transitions as depicted in Fig. 5, (*Davis & Mott, 1970*; *Tauc, 1968*). The Tauc plots of the absorbance spectra were used to estimate the band gap of A, B and C which lie around 2.77 eV, 2.97 eV and 3.12 eV respectively, which are on the higher side of the reported band gap of bismuth titanate nanocomposites (*Yao et al., 2004*; *Lin et al., 2012*; *He et al., 2014*). It was also evident that the band gap of the samples can be tuned by varying the amount of PEG-6000 added to the precursors during synthesis. The change in band gap can be attributed to oxygen deficiencies that originate at the faces of the nanosheets due to imperfections in atomic

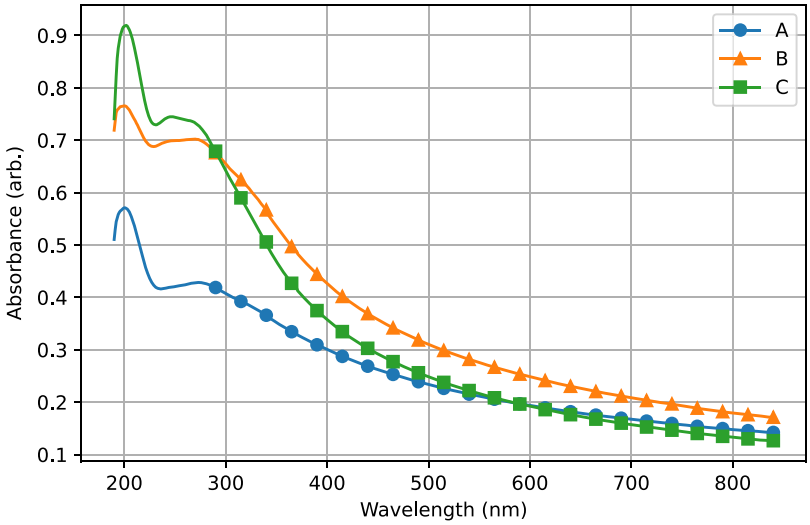

Figure 4 Absorbance spectra of synthesized BTO samples (A), (B) and (C) shows that the samples have increasing absorbance peaks depending on the amount of PEG-6000 added during syntheses. Full-size DOI: 10.7717/peerj-matsci.26/fig-4

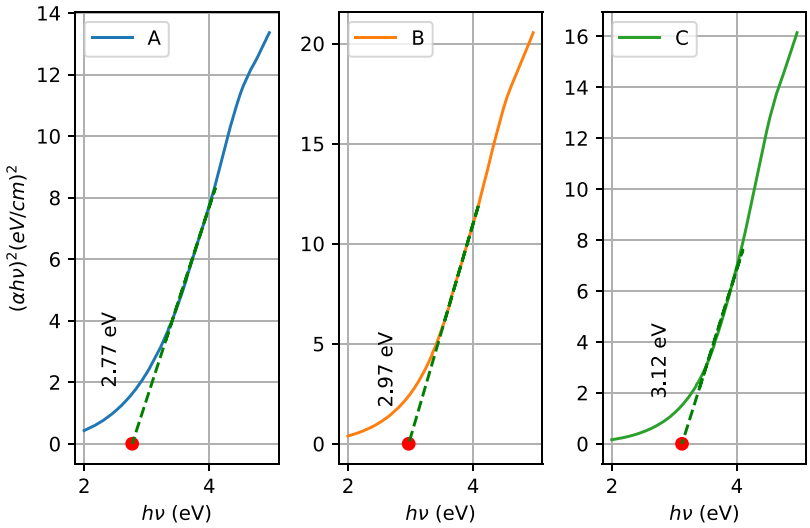

Figure 5 Tauc plots of BTO samples (A), (B) and (C) and the corresponding estimated band gap values, 2.77, 2.97 and 3.12 eV respectively. Given that the known band gap of bulk bismuth titanate in the perovskite form is around 3.1 eV, reduction of thickness of the nanosheets reduces the band gap of the material. Full-size DOI: 10.7717/peerj-matsci.26/fig-5

arrangements. It is assumable that more perfect the crystallite arrangement, the lesser defects are present. This is because the oxygen deficient sites that form at the crystallite faces of the nanosheets due to imperfections in the structure, produce a band of new electronic states, in effect, lowering the band gap of the material. This effect has been seen in action previously in titania and certain bismuth titanates (*Bark, 2013*; *Han & Bark, 2014*; *Choi et al., 2012*; *Badmus et al., 2021*; *Yao et al., 2020*). This in turn brings the band gap of the material closer to the values of pristine bismuth titanate (*Murugesan et al., 2010*).

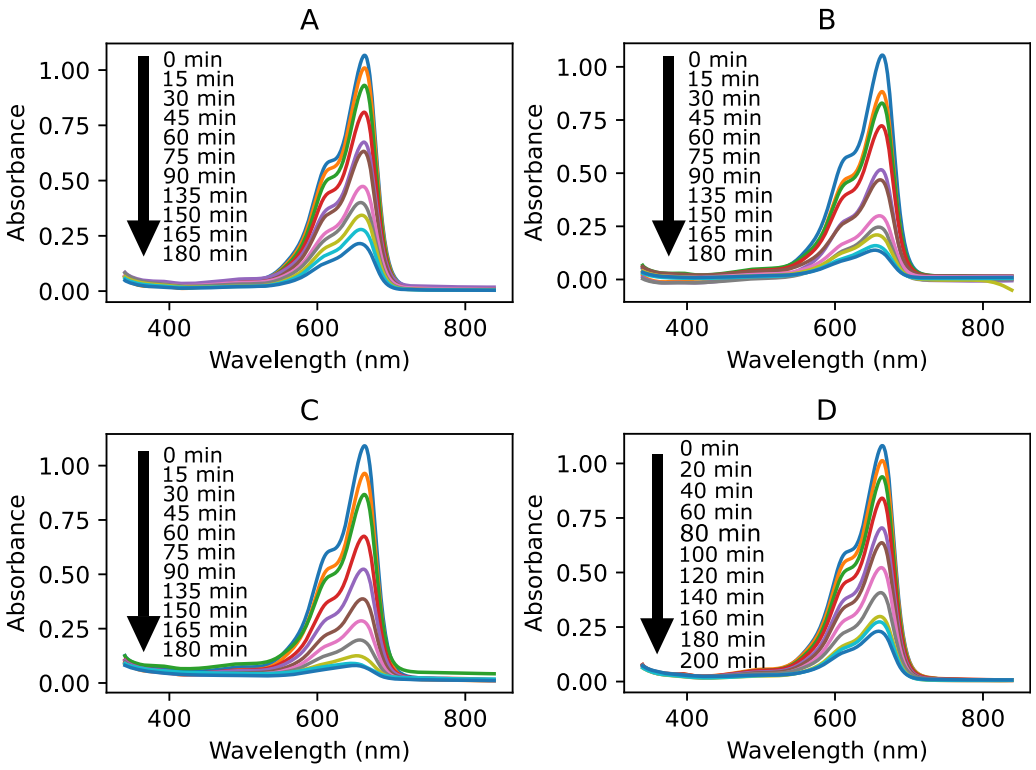

Figure 6 Photodegradation of methylene blue dye measured over its characteristic peak compared with addition of samples (A), (B) and (C) show a final degradation concentration of up to 20.2%, 13.1% and 7.2% respectively, while the dye alone showed a final degradation of 22.1%. Sample A shows lesser photocatalytic efficiency corresponding to its lower absorbance levels.

Full-size DOI: 10.7717/peerj-matsci.26/fig-6

Photocatalysis

The photocatalytic effects of the nanocomposites on the photodegradation of methylene blue dye were studied by irradiating a 1,000 W Xenon lamp on 0.1 µmol of methylene blue dye dissolved in 50 mL of pure water. The dye solution was segregated into five transparent glass containers of 10 mL each. Four of these solutions were added with 5 mg of the samples A, B, C and K. IR irradiation from the lamp was mitigated using a 20 mm block of water that was placed between the sample and the lamp. Photodegradation characteristics of the dye samples with and without the photocatalyst were studied over a period of 100 min by measuring the characteristic absorbance peak of methylene blue dye.
The enhancement of photodegradation caused by dispersing 5 mg each of the synthesized bismuth titanate samples A, B, C and K were recorded and compared to a "blank" MB dye sample D that does not have the photocatalyst. Variation in absorbance of the dye samples were sampled over a span of 180 min. The variation of the characteristic absorbance against time for the dye samples are depicted in Fig. 6.

To calculate the photodegradation characteristics, the variation over time of peak absorbance of methylene blue dye at 653 nm against irradiation time of the samples is plotted. Degradation of the dye improved with the photocatalyst added and the final dye concentration at the 180-min mark reduced to 20.2%, 13.1% and 7.2%, for dye samples

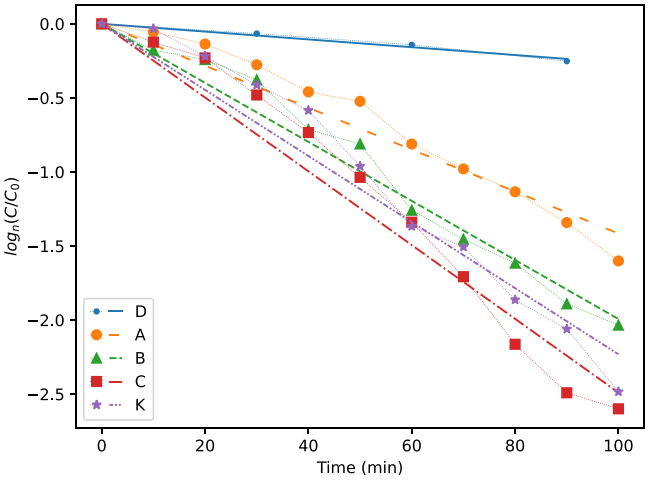

Figure 7 Reaction characteristics of the photodegradation of MB dye catalyzed by BTO samples (A), (B) and (C) depict logarithmic photodegradation. The control sample K has photodegradation characteristics similar to (B) and (C). The markers show experimental data, while the solid lines show straight line fits. Full-size DOI: 10.7717/peerj-matsci.26/fig-7

added with photocatalysts A, B, C respectively. Sample D, which did not have any photocatalyst degraded only up to 77.9%. The control sample K showed degradation close to sample B and C. The logarithmic degradation of the samples was compared, and sample C shows better photocatalysis throughout the 180-min irradiation as shown in Fig. 7.

DISCUSSION

The organic complex formed by the reagents tend to be stabler than both bismuth nitrate pentahydrate and titanium isopropoxide, because of the organic ligands that associate to the metal ions preventing them from reacting to water. The combustion reaction initiated by microwave irradiation tend to form nanosheets of varying thickness and lateral dimensions depending on the amount of PEG added to the precursor. The formation of such sheet structures as well as the mechanism of thickness variation depending on the amount of PEG added would be because the PEG provides a template for the formation nanoparticles. It is well known that PEG tends to aggregate the formed nanoparticles into sheets that extend over tens of nanometers in size (*Zomorodian et al., 2018*; *Yoleva et al., 2011*). As the amount of PEG in the precursor increases, greater number of nucleation occur within the PEG sheets in all directions. As the nuclei grow into nanoparticles, they conform into sheets with thicknesses depending on the nucleation along the z axis. Sample A shows both sheets as well as deformed agglomerates because the amount of PEG required in the precursor for sheet-like nucleation as well as size control is low, resulting in spheroid formations.

An effort towards rationalizing the thickness of the formed nanosheets has been done by estimating the crystallite size along the (001) direction using XRD. This is typically done by applying the Debye-Scherrer equation on the (001) plane. Since the (001) peak was barely measurable, the FHWM as well as height of the XRD peak of the more prominent (002) plane was used for this estimation. The crystallite sizes estimated corresponds to the

half-point of the crystal plane (*Kim et al., 2001*; *Holder & Schaak, 2019*). The samples A, B, and C are overestimated to have approximate crystallite sizes less than 7.0, 8.1 and 9.1 nm respectively (*Monshi, 2012*). Given that various minor peaks add towards the total FWHM, the estimated sizes should be considered higher especially for sample A.

The photodegradation experiment was conducted for an indicative comparison of the variation of efficacies between the synthesized samples. The reaction kinetics of the photodegradation follows a first order nature which has been verified by fitting the variation of absorbance of the characteristic peak of the dye to the equation $log_n(C/C_0) = -kt$, where C_0 is the absorbance value at the beginning of the experiment and C is the variation in absorbance value over time t of reaction (*Xiao et al., 2013*; *Aarthi & Madras, 2007*). Since the physical parameters are only slightly varied between the samples, the photodegradation effect can be attributed mainly to the enhancement in the absorbance which is evident in the absorbance spectra of the samples in Fig. 4. Sample A has the lowest photodegradation coefficient of the lot owing to its lower absorbance characteristics.

CONCLUSIONS

Perovskite bismuth titanate nanosheets were synthesized from bismuth and titanium precursors in a microwave-initiated combustion method. The resulting nanocomposite had less than 7% estimated bismuth oxide phases. Nanosheet morphology was confirmed with an average lateral dimensions of range 100 to 200 nm. The thickness of the nanosheets were varied by the addition of polyethylene glycol during synthesis, which in turn affects the band gap of the material. The photodegradation reaction of methylene blue dye with the BTO samples followed a logarithmic degradation. The sample synthesized by adding 0.06 g of PEG has optimum characteristics to improve photocatalytic effects than samples with 0.02 and 0.04 g of PEG.

ACKNOWLEDGEMENTS

The authors acknowledge the Sophisticated Analytical Instruments Facility, Kochi, India for the necessary facility provided various characterizations.

ADDITIONAL INFORMATION AND DECLARATIONS

Funding

The authors received no funding for this work.

Competing Interests

The authors declare that they have no competing interests.

Author Contributions

- Adrine Antony Correya conceived and designed the experiments, performed the experiments, analyzed the data, performed the computation work, prepared figures and/or tables, authored or reviewed drafts of the article, and approved the final draft.

- V. P. N. Nampoori analyzed the data, authored or reviewed drafts of the article, and approved the final draft.
- A. Mujeeb conceived and designed the experiments, authored or reviewed drafts of the article, and approved the final draft.

Data Availability

The following information was supplied regarding data availability:

The raw data of the experiment and analysis is available at GitHub: https://github.com/acorreya/bto-mw-photocatal; acorreya. (2022). acorreya/bto-mw-photocatal: Raw Data - Microwave assisted synthesis of bismuth titanate nanosheets and its photocatalytic effects (ExperimentalData). Zenodo. https://doi.org/10.5281/zenodo.7395975.

REFERENCES

Aarthi T, Madras G. 2007. Photocatalytic degradation of rhodamine dyes with nano-TiO_2. *Industrial & Engineering Chemistry Research* **46(1)**:7–14 DOI 10.1021/ie060948n.

Aurivillius B. 1949. Mixed bismuth oxides with layer lattices. II. Structure of $Bi_4Ti_3O_{12}$. *Arkiv foer Kemi* **1**:499–512.

Badmus KO, Wewers F, Al-Abri M, Shahbaaz M, Petrik LF. 2021. Synthesis of oxygen deficient TiO_2 for improved photocatalytic efficiency in solar radiation. *Catalysts* **11(8)**:904 DOI 10.3390/catal11080904.

Bakshi MS. 2015. How surfactants control crystal growth of nanomaterials. *Crystal Growth & Design* **16(2)**:1104–1133 DOI 10.1021/acs.cgd.5b01465.

Bark CW. 2013. Structural and optical properties of bandgap engineered bismuth titanate by cobalt doping. *Metals and Materials International* **19(6)**:1361–1364 DOI 10.1007/s12540-013-0641-1.

Chen Z, Jiang H, Jin W, Shi C. 2016. Enhanced photocatalytic performance over $Bi_4Ti_3O_{12}$ nanosheets with controllable size and exposed {0 0 1} facets for Rhodamine B degradation. *Applied Catalysis B: Environmental* **180(1–3)**:698–706 DOI 10.1016/j.apcatb.2015.07.022.

Chen Z, Li S, Zhang W. 2011. Dye-sensitized solar cells based on $Bi_4Ti_3O_{12}$. *International Journal of Photoenergy* **2011(6346)**:1–6 DOI 10.1155/2011/634147.

Chiang Y, Farrey GW, Soukhojak AN. 1998. Lead-free high-strain single-crystal piezoelectrics in the alkaline–bismuth–titanate perovskite family. *Applied Physics Letters* **73(25)**:3683–3685 DOI 10.1063/1.122862.

Choi WS, Chisholm MF, Singh DJ, Choi T, Jellison GE, Lee HN. 2012. Wide bandgap tunability in complex transition metal oxides by site-specific substitution. *Nature Communications* **3(1)**:689 DOI 10.1038/ncomms1690.

Cullity BD, Stock SR. 2014. *Elements of X-ray diffraction*. Harlow: Pearson Education Limited.

Davis EA, Mott NF. 1970. Conduction in non-crystalline systems V. Conductivity, optical absorption and photoconductivity in amorphous semiconductors. *Philosophical Magazine* **22(179)**:903–922 DOI 10.1080/14786437008221061.

Dawley JT, Radspinner R, Zelinski BJJ, Uhlmann DR. 2001. Sol-gel derived bismuth titanate thin films with c-axis orientation. *Journal of Sol-Gel Science and Technology* **20(1)**:85–93 DOI 10.1023/A:1008780701687.

Du X, Xu Y, Ma H, Wang J, Li X. 2008. Low-temperature synthesis of bismuth titanate by an aqueous sol-gel method. *Journal of the American Ceramic Society* **91(7)**:2079–2082 DOI 10.1111/j.1551-2916.2007.02014.x.

Han JY, Bark CW. 2014. Control of optical band gap in La doped bismuth titanate with two stage doping. *Molecular Crystals and Liquid Crystals* **597(1)**:37–44 DOI 10.1080/15421406.2014.931786.

Harris CR, Millman KJ, van der Walt SJ, Gommers R, Virtanen P, Cournapeau D, Wieser E, Taylor J, Berg S, Smith NJ, Kern R, Picus M, Hoyer S, van Kerkwijk MH, Brett M, Haldane A, del Río JF, Wiebe M, Peterson P, Gérard-Marchant P, Sheppard K, Reddy T, Weckesser W, Abbasi H, Gohlke C, Oliphant TE. 2020. Array programming with NumPy. *Nature* **585(7825)**:357–362 DOI 10.1038/s41586-020-2649-2.

Hashimoto K, Irie H, Fujishima A. 2005. TiO_2 photocatalysis: a historical overview and future prospects. *Japanese Journal of Applied Physics* **44(12)**:8269–8285 DOI 10.1143/JJAP.44.8269.

He H, Yin J, Li Y, Zhang Y, Qiu H, Xu J, Xu T, Wang C. 2014. Size controllable synthesis of single-crystal ferroelectric $Bi_4Ti_3O_{12}$ nanosheet dominated with {0 0 1} facets toward enhanced visible-light-driven photocatalytic activities. *Applied Catalysis B: Environmental* **156–157(16)**:35–43 DOI 10.1016/j.apcatb.2014.03.003.

Holder CF, Schaak RE. 2019. Tutorial on powder X-ray diffraction for characterizing nanoscale materials. *ACS Nano* **13(7)**:7359–7365 DOI 10.1021/acsnano.9b05157.

Hunter JD. 2007. Matplotlib: a 2D graphics environment. *Computing in Science & Engineering* **9(3)**:90–95 DOI 10.1109/MCSE.2007.55.

Khan MM, Adil SF, Al-Mayouf A. 2015. Metal oxides as photocatalysts. *Journal of Saudi Chemical Society* **19(5)**:462–464 DOI 10.1016/j.jscs.2015.04.003.

Kim JY, Chung I, Choy JH, Park GS. 2001. Macromolecular nanoplatelet of aurivillius-type layered perovskite oxide, $Bi_4Ti_3O_{12}$. *Chemistry of Materials* **13(9)**:2759–2761 DOI 10.1021/cm0102436.

Kong L, Chen H, Hua W, Zhang S, Chen J. 2008. Mesoporous bismuth titanate with visible-light photocatalytic activity. *Chemical Communications* **359(40)**:4977–4979 DOI 10.1039/b808911f.

Koroleva MS, Piir IV, Ryabkov YI, Korolev DA, Chezhina NV. 2013. Synthesis and properties of chromium-containing bismuth titanates with the pyrochlore structure. *Russian Chemical Bulletin* **62(2)**:408–411 DOI 10.1007/s11172-013-0054-9.

Kubiak A, Bielan Z, Bartkowiak A, Gabała E, Piasecki A, Zalas M, Zielińska-Jurek A, Janczarek M, Siwińska-Ciesielczyk K, Jesionowski T. 2020. Synthesis of titanium dioxide via surfactant-assisted microwave method for photocatalytic and dye-sensitized solar cells applications. *Catalysts* **10(5)**:586 DOI 10.3390/catal10050586.

Lanfredi S, Nobre MAL. 2005. Conductivity mechanism analysis at high temperature in bismuth titanate: a single crystal with sillenite-type structure. *Applied Physics Letters* **86(8)**:81916 DOI 10.1063/1.1869542.

Langford JI, Wilson AJC. 1978. Seherrer after sixty years: a survey and some new results in the determination of crystallite size. *Journal of Applied Crystallography* **11**:12 DOI 10.1107/S0021889878012844.

Lazarević Z, Stojanović BD, Varela JA. 2005. An approach to analyzing synthesis, structure and properties of bismuth titanate ceramics. *Science of Sintering* **37(3)**:199–216 DOI 10.2298/SOS0503199L.

Lin X, Lv P, Guan Q, Li H, Zhai H, Liu C. 2012. Bismuth titanate microspheres: directed synthesis and their visible light photocatalytic activity. *Applied Surface Science* **258(18)**:7146–7153 DOI 10.1016/j.apsusc.2012.04.019.

Lutterotti L. 2012. Full profile search match of diffraction patterns using the crystallography open database of structures. *Available at http://nanoair.dii.unitn.it:8080/sfpm/*.

Lutterotti L, Bortolotti M, Ischia G, Lonardelli I, Wenk HR. 2007. Rietveld texture analysis from diffraction images. *Zeitschrift für Kristallographie Supplements* **2007(suppl_26)**:125–130 DOI 10.1524/zksu.2007.2007.suppl_26.125.

Lutterotti L, Pillière H, Fontugne C, Boullay P, Chateigner D. 2019. Full-profile search-match by the Rietveld method. *Journal of Applied Crystallography* **52(3)**:587–598 DOI 10.1107/S160057671900342X.

Maji SK, Mukherjee N, Mondal A, Adhikary B. 2012. Synthesis, characterization and photocatalytic activity of α-Fe_2O_3 nanoparticles. *Polyhedron* **33(1)**:145–149 DOI 10.1016/j.poly.2011.11.017.

Monshi A. 2012. Modified scherrer equation to estimate more accurately nano-crystallite size using XRD. *World Journal of Nano Science and Engineering* **2(3)**:154–160 DOI 10.4236/wjnse.2012.23020.

Murugesan S, Huda MN, Yan Y, Al-Jassim MM, Subramanian V. 2010. Band-engineered bismuth titanate pyrochlores for visible light photocatalysis. *Journal of Physical Chemistry C* **114(23)**:10598–10605 DOI 10.1021/jp906252r.

Natarajan TS, Natarajan K, Bajaj HC, Tayade RJ. 2013. Enhanced photocatalytic activity of bismuth-doped TiO_2 nanotubes under direct sunlight irradiation for degradation of Rhodamine B dye. *Journal of Nanoparticle Research* **15(5)**:942 DOI 10.1007/s11051-013-1669-3.

Newnham RE, Wolfe RW, Dorrian JF. 1971. Structural basis of ferroelectricity in the bismuth titanate family. *Materials Research Bulletin* **6(10)**:1029–1039 DOI 10.1016/0025-5408(71)90082-1.

Nogueira AE, Longo E, Leite ER, Camargo ER. 2014. Synthesis and photocatalytic properties of bismuth titanate with different structures via oxidant peroxo method (OPM). *Journal of Colloid and Interface Science* **415**:89–94 DOI 10.1016/j.jcis.2013.10.010.

Noureldine D, Lardhi S, Ziani A, Harb M, Cavallo L, Takanabe K. 2015. Combined experimental-theoretical study of the optoelectronic properties of non-stoichiometric pyrochlore bismuth titanate. *Journal of Materials Chemistry C* **3(46)**:12032–12039 DOI 10.1039/C5TC03134F.

Park JH, Park OO, Kim S. 2006. Photoelectrochemical water splitting at titanium dioxide nanotubes coated with tungsten trioxide. *Applied Physics Letters* **89(16)**:163106 DOI 10.1063/1.2357878.

Perez F, Granger BE. 2007. IPython: a system for interactive scientific computing. *Computing in Science & Engineering* **9(3)**:21–29 DOI 10.1109/MCSE.2007.53.

Pirgholi-Givi G, Farjami-Shayesteh S, Azizian-Kalandaragh Y. 2019. The influence of preparation parameters on the photocatalytic performance of mixed bismuth titanate-based nanostructures. *Physica B: Condensed Matter* **575**:311572 DOI 10.1016/j.physb.2019.07.007.

Ramana EV, Prasad NV, Tobaldi DM, Zavašnik J, Singh MK, Hortigüela MJ, Seabra MP, Prasad G, Valente MA. 2017. Effect of samarium and vanadium co-doping on structure, ferroelectric and photocatalytic properties of bismuth titanate. *RSC Advances* **7(16)**:9680–9692 DOI 10.1039/C7RA00021A.

Sardar K, Walton RI. 2012. Hydrothermal synthesis map of bismuth titanates. *Journal of Solid State Chemistry* **189**:32–37 DOI 10.1016/j.jssc.2012.01.017.

Skorikov VM, Kargin YF, Egorysheva AV, Volkov VV, Gospodinov M. 2005. Growth of sillenite-structure single crystals. *Inorganic Materials* **41(S1)**:S24–S46 DOI 10.1007/s10789-005-0317-4.

Sunada K, Kikuchi Y, Hashimoto K, Fujishima A. 1998. Bactericidal and detoxification effects of TiO_2 thin film photocatalysts. *Environmental Science and Technology* **32(5)**:726–728 DOI 10.1021/es970860o.

Tauc J. 1968. Optical properties and electronic structure of amorphous Ge and Si. *Materials Research Bulletin* **3(1)**:37–46 DOI 10.1016/0025-5408(68)90023-8.

Thiruramanathan P, Sharma SK, Sankar S, Sankar Ganesh R, Marikani A, Kim DY. 2016. Synthesis of bismuth titanate (BTO) nanopowder and fabrication of microstrip rectangular patch antenna. *Applied Physics A: Materials Science and Processing* **122(12)**:811 DOI 10.1007/s00339-016-0549-y.

Wei W, Dai Y, Huang B. 2009. First-principles characterization of bi-based photocatalysts: $Bi_{12}TiO_{20}$, $Bi_2Ti_2O_7$, and $Bi_4Ti_3O_{12}$. *The Journal of Physical Chemistry C* **113(14)**:5658–5663 DOI 10.1021/jp810344e.

Xiao X, Hu R, Liu C, Xing C, Qian C, Zuo X, Nan J, Wang L. 2013. Facile large-scale synthesis of β-Bi_2O_3 nanospheres as a highly efficient photocatalyst for the degradation of acetaminophen under visible light irradiation. *Applied Catalysis B: Environmental* **140–141**:433–443 DOI 10.1016/j.apcatb.2013.04.037.

Yang Z, Fan H, Wang X, Long C. 2013. Rapid microwave-assisted hydrothermal synthesis of $Bi_{12}TiO_{20}$ hierarchical architecture with enhanced visible-light photocatalytic activities. *Journal of Physics and Chemistry of Solids* **74(12)**:1739–1744 DOI 10.1016/j.jpcs.2013.06.020.

Yao L, Chen Z, Li J, Shi C. 2020. Creation of oxygen vacancies to activate lanthanum-doped bismuth titanate nanosheets for efficient synchronous photocatalytic removal of Cr(VI) and methyl orange. *Journal of Molecular Liquids* **314**:113613 DOI 10.1016/j.molliq.2020.113613.

Yao WF, Wang H, Xu XH, Shang SX, Hou Y, Zhang Y, Wang M. 2003. Synthesis and photocatalytic property of bismuth titanate $Bi_4Ti_3O_{12}$. *Materials Letters* **57(13–14)**:1899–1902 DOI 10.1016/S0167-577X(02)01097-2.

Yao WF, Xu XH, Wang H, Zhou JT, Yang XN, Zhang Y, Shang SX, Huang BB. 2004. Photocatalytic property of perovskite bismuth titanate. *Applied Catalysis B: Environmental* **52(2)**:109–116 DOI 10.1016/j.apcatb.2004.04.002.

Yi SW, Kim SS, Kim JW, Jo HK, Do D, Kim WJ. 2009. Multiferroic properties of $BiFeO_3$/$Bi_4Ti_3O_{12}$ double-layered thin films fabricated by chemical solution deposition. *Thin Solid Films* **517(24)**:6737–6741 DOI 10.1016/j.tsf.2009.05.029.

Yoleva A, Djambazov S, Ivanova Y, Kashchieva E. 2011. Sol-gel synthesis of titanate phases from aurivillius and sillenite type ($Bi_4Ti_3O_{12}$ and $Bi_{12}TiO_{20}$). *Chemical Technology* 255–260.

Zambrano P, Sayagués MJJ, Navío JAA, Hidalgo MCC. 2017. Outstanding visible photocatalytic activity of a new mixed bismuth titanatate material. *Applied Surface Science* **394**:16–24 DOI 10.1016/j.apsusc.2016.10.042.

Zarycka A, Lisińska-Czekaj A, Czuber J, Orkisz T, Ilczuk J, Czekaj D. 2005. The sol-gel synthesis of bismuth titanate electroceramic thin films. *Materials Science-Poland* **23(1)**.

Zhao W, Jia Z, Lei E, Wang L, Li Z, Dai Y. 2013. Photocatalytic degradation efficacy of $Bi_4Ti_3O_{12}$ micro-scale platelets over methylene blue under visible light. *Journal of Physics and Chemistry of Solids* **74(11)**:1604–1607 DOI 10.1016/j.jpcs.2013.06.003.

Zhao ZG, Miyauchi M. 2008. Nanoporous-walled tungsten oxide nanotubes as highly active visible-light-driven photocatalysts. *Angewandte Chemie International Edition* **47(37)**:7051–7055 DOI 10.1002/anie.200802207.

Zhou J, Zou Z, Ray AK, Zhao XS. 2007. Preparation and characterization of polycrystalline bismuth titanate $Bi_{12}TiO_{20}$ and its photocatalytic properties under visible light irradiation. *Industrial and Engineering Chemistry Research* **46(3)**:745–749 DOI 10.1021/ie0613220.

Zomorodian K, Veisi H, Mousavi M, Ataabadi M, Yazdanpanah S, Bagheri MJ, Mehr A, Hemmati S, Veisi H. 2018. Modified magnetic nanoparticles by PEG-400-immobilized Ag nanoparticles (Fe_3O_4@PEG–Ag) as a core/shell nanocomposite and evaluation of its antimicrobial activity. *International Journal of Nanomedicine* **13**:3965–3973 DOI 10.2147/IJN.S161002.